Study of the optical properties of $Sb_2(Se_{1-x}S_x)_3$ (x = 0–1) solid solutions

Mehmet Ender Uslu [a,*], Rokas Kondrotas [b], Ramūnas Nedzinskas [b], Olga Volobujeva [a], Kristi Timmo [a], Marit Kauk-Kuusik [a], Jüri Krustok [a], Maarja Grossberg [a]

[a] Department of Materials and Environmental Technology, Tallinn University of Technology, Ehitajate tee 5, 19086, Tallinn, Estonia
[b] State Research Institute Center for Physical Sciences and Technology, Saulètekio Ave. LT-10257, Vilnius, Lithuania

ARTICLE INFO

ABSTRACT

This study presents a detailed analysis of the optical properties of the $Sb_2(Se_{1-x}S_x)_3$ (x = 0–1) polycrystals. Four antimony selenosulfide solid solutions $Sb_2(Se_{1-x}S_x)_3$ together with Sb2Se3 and Sb2S3 were synthesized from elemental precursors at the same synthesis conditions, only varying the x = S/(Se + S) value with a step of $\Delta x = 0.2$. Successful formation of the $Sb_2(Se_{1-x}S_x)_3$ solid solutions was determined by Raman spectroscopy and X-ray diffraction. As expected for the same type of crystal structure of Sb_2Se_3 and Sb_2S_3, the bimodal behavior of A_g Raman mode in $Sb_2(Se_{1-x}S_x)_3$ was detected. Temperature and excitation power dependent photoluminescence (PL) analysis of $Sb_2(Se_{1-x}S_x)_3$ was performed in order to look into the electronic and defect structure of these promising semiconductor materials for optoelectronic applications. The shift of the near band edge PL emission in $Sb_2(Se_{1-x}S_x)_3$ towards higher energies from 1.309 eV to 1.728 eV with increasing sulfur content was detected at T = 3 K. A change in the radiative recombination mechanism was detected being of excitonic origin in samples with x ≤ 0.2 and resulting from deep donor-deep acceptor pair recombination in samples with x > 0.2.

1. Introduction

Antimony chalcogenides (Sb_2Ch_3), where Ch refers to S, Se, or Te, find widespread practices in photocatalysis, supercapacitors, and photovoltaics, as exhibiting thermoelectric [1,2], photoelectric, and dielectric [3] features. One of the most promising chalcogenides for photoelectric applications is the antimony selenide that was first introduced in the 1950s [4]. Antimony selenide (Sb_2Se_3) is a binary compound from the V_2-VI_3 group with anisotropic optoelectronic properties. It gained research attention in the last decade as an absorber material in thin-film solar cells due to an optimal band gap energy of 1.2 eV at room temperature [5], a high absorption coefficient of 10^4 cm^{-1} at visible wavelengths [6], and due to being a relatively cheap material composed of earth abundant elements with low toxicity.

However, Sb_2Se_3 has a quasi-1D ribbons-like crystal structure, which results in 3 and 2 non-equivalent lattice sites for Se and Sb, respectively. Such low symmetry configuration of atoms in the lattice leads to large variety of point defects and complicated defect chemistry overall [7–9]. Complex defects with unknown nature may act as recombination centers, which drastically degrade the photoelectric conversion efficiency of the respective devices. Although the thermal activation of free electrons or holes benefits from specific intrinsic defects, not every kind of defect

has an off-stoichiometric doping character. A recent computational study using the hybrid method in Density Functional Theory (DFT) suggests that in Sb_2Se_3 there are low formation energy cation–anion antisite defects with mid-gap transition levels that could act as recombination centers [10]. Briefly, these deep defects can be the main drawback against the advancement of Sb_2Se_3 based thin-film solar cells. The maximum power conversion efficiency of antimony selenide-based solar cells so far is 9.2% [11], resulting from enhanced current density due to improved alignment of the crystals in [221] and [211] directions enabling more efficient charge-carriers transport. The grain boundaries between the ribbons stacked together by Van der Waals forces act as obstructive spaces degrading charge-carriers transport in [hk0] directions [12]. In other words, the anisotropic crystal structure is the second limiting factor for the energy conversion efficiency of the Sb_2Se_3 photoabsorber.

The most accepted consensus in the literature about Sb_2Se_3 based thin-film solar cells is that a Se-rich composition, where Se replaces some Sb-sites (Se_{Sb}), enhances p-type conductivity, and increases the power conversion efficiency [13]. However, the post-growth selenization process, which is usually used to obtain a Se-rich Sb_2Se_3, has been shown to result only in a slight increment of Se-content since antimony selenide has a single-phase structure with no stable secondary phase.

The need for the post-growth selenization can also be due to the volatility of selenium in high-temperature processes during the deposition of Sb_2Se_3 by methods like rapid thermal evaporation (RTE) [14], close spaced sublimation (CSS) [15], and vapor transfer deposition (VTD). Nevertheless, experiments, which were performed to reveal the dominant defects in Sb_2Se_3, synthesized by different methods, show different results depending on the crystal quality, and slight deviations from stoichiometry. A deep-level transient spectroscopy (DLTS) study of a Sb_2Se_3 based thin-film solar cell confirmed the existence of the deep defects with the nature of hole traps at around 0.48 eV and 0.71 eV above the valence band maximum (VBM), respectively, assigned to V_{Sb} and Se_{Sb} [16]. On the other hand, the low-temperature (T = 10 K) photoluminescence (PL) spectra of Sb_2Se_3 polycrystals showed three bands at 0.94, 1.10, and 1.24 eV [17]. The authors confirmed the emission at 0.94 eV as evidence of the close donor-acceptor pair (DAP) recombination, while the one at 1.24 eV resulting from distant donor-acceptor pair recombination. In addition to this, temperature and laser power-dependent PL study of Sb_2Se_3 microcrystals using pulsed UV laser reported near band-edge excitons and biexcitons [18]. In Sb_2S_3 the band-to-band PL emission was detected at 1.65 eV at room temperature and its intensity was found to change noticeably depending on the deposition method [19].

The optical processes in Sb_2Se_3 are also affected by the closely positioned direct and indirect band-gaps [6]. Apart from this, also the valence band splitting by a crystal field (Δ_{cr} = 13 meV) and the spin-orbit interaction (Δ_{so} = 35 meV) at the Brillouin zone center has been detected [20]. It is crucial to collect more information about the electronic band structure of such highly anisotropic semiconductor material. Moreover, Sb_2Se_3 is isomorphous to antimony sulfide (Sb_2S_3) as both are from *Pnma(62)* space group [21], so we can follow a strategy of varying the x = S/(S + Se) value in $Sb_2(Se_{1-x}S_x)_3$ solid solutions to learn more about the electronic structure of this promising group of materials. Varying the x-value enables to tune the bandgap of $Sb_2(Se_{1-x}S_x)_3$ in the range from 1.2 eV to 1.7 eV broadening the field of applications of these materials [22]. Moreover, $Sb_2(Se_{1-x}S_x)_3$ (with determined Se content of 29 at%) based thin film solar cells have demonstrated power conversion efficiencies above $\sim$ 10% [23]. The optical properties of the $Sb_2(Se_{1-x}S_x)_3$ solid solutions are barely studied and there is no photoluminescence data available for this material series. Therefore, this study aims at detailed insight into the electronic and defect structure of $Sb_2(Se_{1-x}S_x)_3$ solid solutions (x varying from 0 to 1 and with Δx = 0.2) using excitation power density and temperature dependent PL measurements to improve the understanding of the fundamental properties of these promising absorber materials for photovoltaics.

2. Experimental

$Sb_2(Se_{1-x}S_x)_3$ solid solutions with x = 0, 0.2, 0.4, 0.6, 0.8 and 1 were synthesized from 5 N purity Sb, Se and S (Alfa Aesar) elemental precursors at the same synthesis conditions. The precursors were weighed in desired amounts and ratios, mixed and ground in an agate mortar, loaded into quartz ampoules, degassed and sealed under dynamic vacuum. For the synthesis, a two-step isothermal annealing process in a chamber furnace was used. All six samples together were heated up from room temperature to 200 °C within 1 h. After one week at 200 °C, the temperature was increased from 200 °C to 500 °C within 1 h. The samples were kept at 500 °C for one week. After two weeks, the synthesis-growth processes were stopped by taking the ampoules out of the furnace and cool down naturally in air to room temperature.

The elemental composition of the synthesized polycrystals were determined by Energy Dispersive X-ray Spectroscopy (EDX) using a Bruker Esprit 1.8 system on Zeiss Merlin high-resolution Scanning Electron Microscope (SEM). The phase composition and the evolution of the solid solution formation with varying S/Se ratio in $Sb_2(Se_{1-x}S_x)_3$ was studied by using room-temperature micro-Raman analysis with Horiba's

LabRam HR800 spectrometer with a 532 nm laser line and with the spot size of 5 μm in diameter. The Raman analysis was complemented by the powder X-Ray Diffraction (XRD) analysis using Rigaku Ultima IV diffractometer operating with the silicon strip detector D/teX Ultra. PDXL 2 software was used for the derivation of crystal structure information from the powder XRD data (ICDD 01-083-7430 and 03-065-2434 for Sb_2Se_3 and Sb_2S_3, respectively).

For the PL measurements the polycrystals were mounted on the cold finger of a closed-cycle helium cryostat Janis SHI-4 of Lake Shore Cryotronics and the measurements were carried out in the temperature region of 3–110 K. Near band edge PL spectra were excited with a diode-pumped Nd:YAG solid state laser with the wavelength of 266 nm, pulse width 0.6 ns, and repetition rate 19 kHz. The maximum peak energy was 0.75 μJ and the maximum average power was approximately 15 mW. The maximum peak power density was estimated to be 660 kW cm^{-2}. The laser beam was not focused to avoid damaging the sample and the pump power was reduced by a gradient UV (fused silica) filter. The PL signal was dispersed using a 0.5 m focal length Andor SR-500i monochromator and captured with thermoelectrically cooled InGaAs detector IGA-030-TE2-H of Electro-Optical Systems Inc and with Hamamatsu R632 photomultiplier tube in the case of Sb_2S_3.

For comparison, the PL spectra of deeper bands in the $Sb_2(Se_{1-x}S_x)_3$ polycrystals were also measured by using a continuous wave He–Cd gas laser (Kimmon) with a wavelength of 442 nm and maximum power of 37.1 mW. For the respective measurements, the samples were mounted on the cold finger of a closed-cycle helium cryostat (Janis CCS-150) and cooled down to 20 K. For PL signal detection, a Hamamatsu InGaAs photomultiplier tube was used in the range of 0.77–1.35 eV.

3. Results and discussion

Average values of multiple spots from each polycrystalline solid solution measured by the EDX microanalysis are shown in Table 1. The results confirm the aimed elemental compositions of $Sb_2(Se_{1-x}S_x)_3$ (x varying from 0 to 1 and with $\Delta x \sim$ 0.2). Evolution of the Raman spectra and XRD patterns with x-value in $Sb_2(Se_{1-x}S_x)_3$ are presented in Figs. 1 and 2. The experimental Raman spectra were fitted with the Lorentzian functions. The Raman spectra of the pure Sb_2Se_3 and Sb_2S_3 compounds are in a very good correlation to the literature data with dominating A_g^2 mode at 190 cm^{-1} accompanied with other modes at 100, 125, 156, 213

Table 1
Elemental compositions of the studied $Sb_2(Se_{1-x}S_x)_3$ solid solutions determined by EDX.

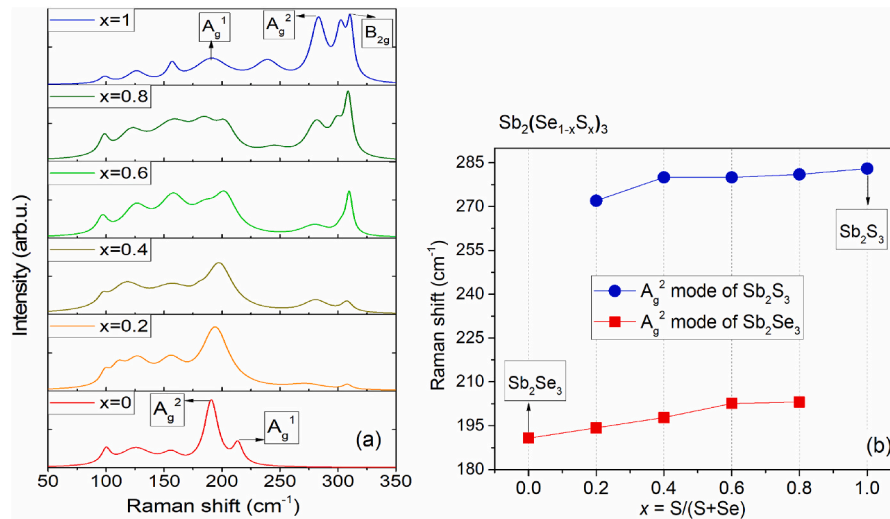| $Sb_2(Se_{1-x}S_x)_3$	x= S/(S + Se) input	x= S/(S + Se) outcome	Antimony (Sb)	Selenium (Se)	Sulfur (S)
Sb_2Se_3	x = 0	x = 0	40.1 at% ±1.4 at%	59.8 at% ±1.4 at%	–
$Sb_2(Se_{0.8}S_{0.2})_3$	x = 0.2	x = 0.21	40.2 at% ±1.5 at%	46.8 at% ±1.2 at%	12.9 at% ±0.2 at%
$Sb_2(Se_{0.6}S_{0.4})_3$	x = 0.4	x = 0.38	39.9 at% ±1.6 at%	36.8 at% ±1.0 at%	23.2 at% ±0.3 at%
$Sb_2(Se_{0.4}S_{0.6})_3$	x = 0.6	x = 0.60	40.1 at% ±1.7 at%	23.8 at% ±0.7 at%	35.9 at% ±0.5 at%
$Sb_2(Se_{0.2}S_{0.8})_3$	x = 0.8	x = 0.81	40.1 at% ±1.8 at%	10.8 at% ±0.3 at%	49 at% ±0.7 at%
Sb_2S_3	x = 1	x = 1	40.2 at% ±1.9 at%	–	59.8 at% ±0.9 at%

Fig. 1. **a)** Raman spectra of $Sb_2(Se_{1-x}S_x)_3$ solid solutions, **b)** bimodal behavior of the A_g^2 Raman modes regarding the x-value.
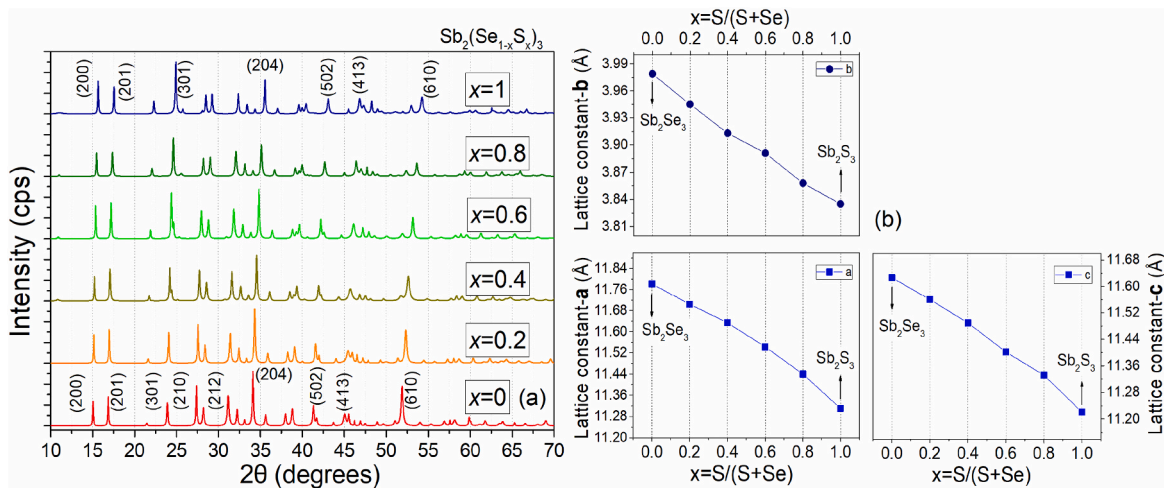

Fig. 2. a) XRD patterns of $Sb_2(Se_{1-x}S_x)_3$ solid solutions, as the x changes from 0 to 1, b) the change in lattice constants for solid solutions depending on the x-value.

cm^{-1} in Sb_2Se_3 [24], and at A_g^2 mode of Sb_2S_3 at 283 cm^{-1} accompanied with the other modes at 98, 125, 156, 190, 239, 310 cm^{-1} [25,26]. The bimodal behavior of A_g^2 modes confirms the formation of the $Sb_2(Se_{1-x}S_x)_3$ solid solutions (see Fig. 1a and b) although two Raman studies of Sb_2S_3, under different polarization, pressure and temperature conditions, report different position of an A_g mode at 312 cm^{-1} [25] and B_{2g} mode at 314 cm^{-1} [26]. The behavior of FWHM on x value for two main peaks is given in Fig. S1. The XRD patterns of the solid solutions in Fig. 2a with x changing from 0 to 1, show that all the peaks belong to Sb_2Se_3 and Sb_2S_3, respectively, and to their solid solutions. All of the
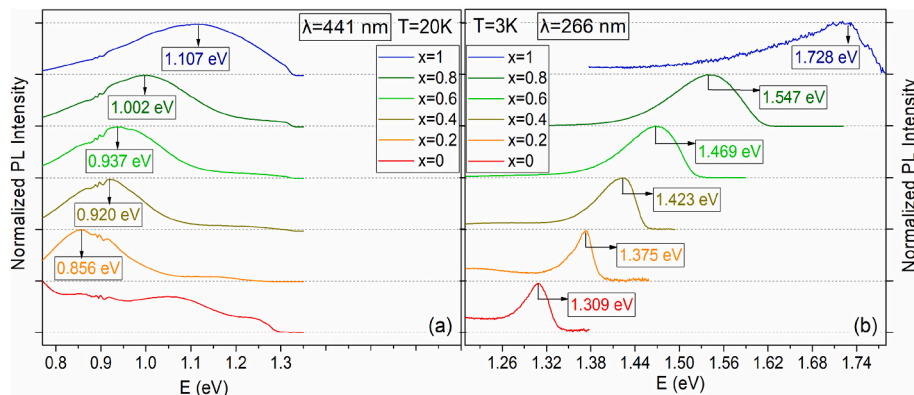

Fig. 3. **a)** PL spectra of the $Sb_2(Se_{1-x}S_x)_3$ solid solutions with x varying from 0 to 1, respectively, excited by continuous wave laser (441 nm) at T = 20 K. **b)** PL spectra of the same materials excited by the pulsed UV laser (266 nm) at T = 3 K and laser power of 15 mW.

solid solutions were determined to have an orthorhombic structure with space group *Pnma*. A shift of the XRD peaks towards higher degrees with increasing x-value was detected. The lattice parameters for each solid solution were extracted using Rietveld refinement procedure and the corresponding values regarding the x-value are shown in Fig. 2b. An example of the Rietveld refinement for one sample is given in Table S1 and Table S2. Decrease in the lattice parameters with increasing x value is detected as expected due to the smaller size of S atoms.

In order to study the electronic and defect structure of the $Sb_2(Se_{1-x}S_x)_3$ solid solutions, temperature and laser power dependent photoluminescence measurements were performed and analyzed. The low-temperature (T = 3 K) near band edge PL spectra measured with pulsed UV laser are presented in Fig. 3b, from where an asymmetric shape of the PL bands and a shift of the PL emission towards higher energies from 1.309 eV to 1.728 eV with increasing sulfur content is detected. All the detected PL spectra were dominated by an asymmetric PL band, which was fitted with Split-PseudoVoigt function. Fig. 3a presents the PL bands excited with the continuous wave laser at T = 20 K, where the dominating PL band position E_{max} shows a blueshift from 0.856 eV to 1.107 eV with x varying from 0.2 to 1. The dominating PL band of Sb_2Se_3 is out of the measurement range (<0.8 eV). These very broad (FWHM ~ 0.25 eV) and Gaussian shaped deep PL bands have rather low intensity making the reliable detailed temperature and laser power dependent analysis impossible. Since the dependence of the low-temperature PL spectra of the $Sb_2(Se_{1-x}S_x)_3$ solid solutions on the x-value is not available in the literature, it is presented in the current paper. From here we focus on the analysis of the edge PL emission of $Sb_2(Se_{1-x}S_x)_3$ excited with the pulsed UV laser (see Fig. 3b).

Temperature dependencies of the edge PL band positions E_{max} of the $Sb_2(Se_{1-x}S_x)_3$ solid solutions are shown in Fig. 4. Redshift of the PL band position with increasing temperature, which is more rapid than the temperature dependence of the bandgap energy [27], was detected for $Sb_2(Se_{1-x}S_x)_3$ with x = 0 and x = 0.2. Similar rapid redshift was detected in Ref. [18] and was attributed mostly to biexcitons. For the other samples, the redshift could not be observed within the used temperature range, as the PL emission quenched fast and disappeared from T > 60 K. The dependence of the integrated PL intensity Φ (P) as a function of laser power P in the range from 0.1 mW to 15 mW for the $Sb_2(Se_{1-x}S_x)_3$ solid solutions with x varying from 0 to 1 is shown in Fig. 5a and is following the dependence $\Phi \sim P^m$ [28]. The power coefficient values m = 1.37 and m = 1.03 were found for $Sb_2(Se_{1-x}S_x)_3$ with x = 0 and x = 0.2, respectively, indicating to the exciton related recombination processes, which are known to have m ≥ 1. Excitons and biexcitons have been recently detected in high quality Sb_2Se_3 microcrystals under high PL excitation density [18]. However, m < 1 was found for the rest of the $Sb_2(Se_{1-x}S_x)_3$ solid solutions with x = 0.4 to x = 1, indicating to a different type of radiative recombination in the respective samples involving charge carriers localized at defects within the band gap. Interestingly, no shift of the PL band position E_{max} with laser power could be detected for all

studied $Sb_2(Se_{1-x}S_x)_3$ solid solutions.

Looking at the shape of the PL bands, such asymmetric shape at low temperatures can result from an electron–phonon coupling, where phonon replicas follow a Poisson distribution as described by the well-known Frank-Condon configuration coordinate model [29]. This applies for the samples with x > 0.2 as in the case of x ≤ 0.2, the laser power dependence of the PL emission indicated excitonic origin as described above. The asymmetric shape is also characteristic to heavily doped semiconductors, which in this case can be excluded as no characteristic strong blueshift (usually >10 meV/decade) of the PL bands with increasing laser power could be detected [30]. Moreover, theoretical DFT calculations predict high concentration of rather deep donor and acceptor defects in Sb_2Se_3, which easily form deep donor-deep acceptor pairs (DD-DA) [10]. DD-DA pair recombination involving a donor and an acceptor, which are located at very short distance in the crystal lattice includes strong Coulomb interaction between the corresponding defects and can result in close to band edge emission with PL peak energy [31]:

$$E_{DAP} = E_g - (E_A + E_D) + \frac{e^2}{4\pi \cdot \varepsilon \varepsilon_o \cdot r} \qquad 1$$

where E_g is the bandgap energy, E_D and E_A are respectively donor and acceptor ionization energies, ε_o is vacuum permittivity, ε is the relative dielectric constant, and r is the distance between donor and acceptor defect in the crystal lattice. When paired, the ionization energies of the related donor and acceptor defects in the case of closest pairs are rather small. Usually DAP emission is characterized with a small blueshift with increasing laser power (in the order of few meV). However, in the case of very close donor-acceptor pairs, there can be almost no blueshift as is observed also in this study for the $Sb_2(Se_{1-x}S_x)_3$ solid solutions [32].

According to the Frank-Condon configuration coordinate model, the full PL spectrum related to recombination centre consists of zero phonon line and its phonon replicas, which are separated by the phonon energy E_{ph}. The intensity of each phonon replica is proportional to $I(k) \sim \exp(-S)S^k/k!$ [29] with k from 0 to ∞ (see Fig. 6). In quite high quality crystals, the spectral shape of zero phonon line and its phonon replicas is Gaussian with halfwidth w. E_{ph} is usually the longitudinal optical (LO) phonon energy. However, in polycrystalline and anisotropic $Sb_2(Se_{1-x}S_x)_3$ solid solutions the spectral shape of these components can be different. Inhomogeneous broadening of zero phonon line can increase the halfwidth of all peaks and the shape can become asymmetric. Therefore, it is difficult to resolve all individual peaks in our spectra and we just see a total asymmetric band.

The strength of the electron-phonon interaction and therefore the distribution of the phonon replicas is described by the S parameter, which is called a Huang-Rhys factor. In this study, a rather small values, namely S ~0.8 were determined for the studied $Sb_2(Se_{1-x}S_x)_3$ solid solutions. The difference (W_L - W_H) between half-width of the low energy side (W_L) and half-width of the high energy side (W_H) of the PL band was
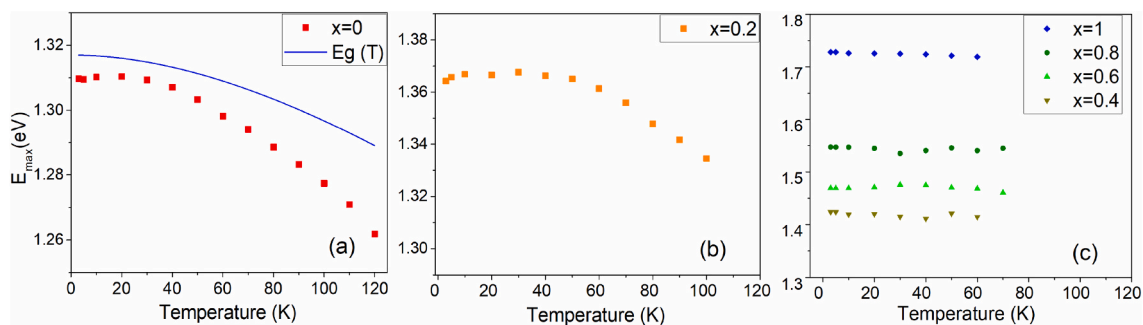

Fig. 4. Temperature dependencies of the PL band positions of the $Sb_2(Se_{1-x}S_x)_3$ solid solutions. $E_g(T)$ is temperature dependence of the bandgap energy of Sb_2Se_3 measured by photoreflectance [27]: **a)** redshift of E_{max} for x = 0, **b)** redshift of E_{max} for x = 0.2, **c)** from x = 0.4 to 1, no clear shift of the peaks could be detected within this temperature range.
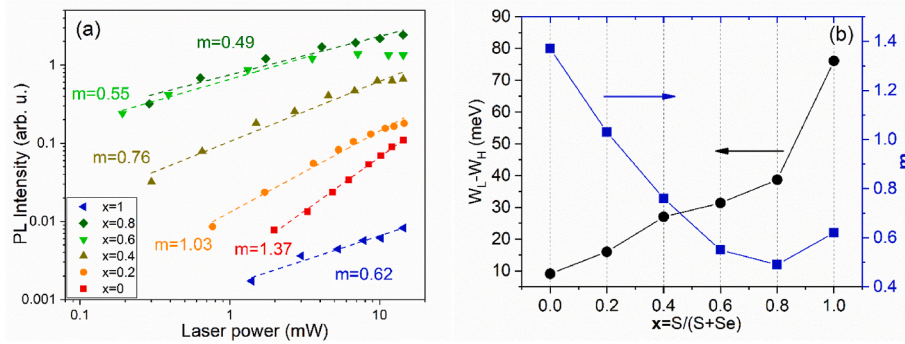
Fig. 5. a) The integrated intensities of near band edge PL bands as a function of laser power at T = 3 K on a log-log scale for the $Sb_2(Se_{1-x}S_x)_3$ solid solutions. **b)** The opposite trends of (W_L-W_H) and m value on the x-value of $Sb_2(Se_{1-x}S_x)_3$ at T = 3 K.
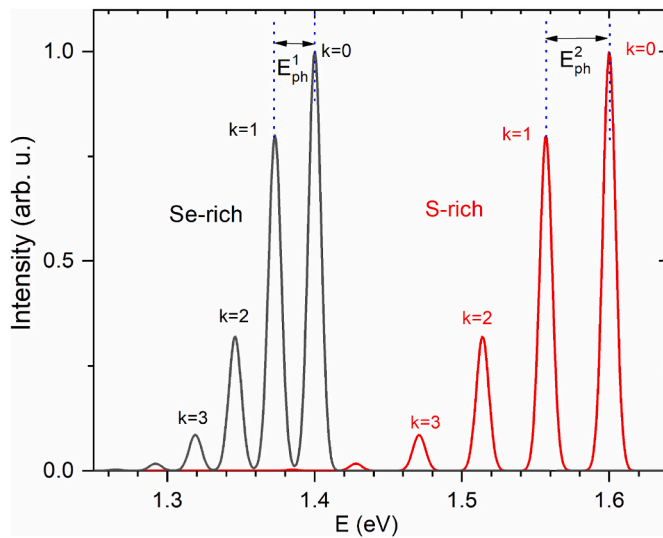

Fig. 6. Theoretical shape of PL bands with different phonon energies and S = 0.8. Gaussian shape with w = 10 meV was used in calculations. The zero phonon line position was taken 1.4 and 1.6 eV for Se-rich and S-rich $Sb_2(Se_{1-x}S_x)_3$ cases, respectively. The asymmetry of resulting PL band is increasing with increase of E_{ph}.

found to grow linearly with increasing sulfur content (see Fig. 5b).

The increased asymmetry of the PL band with increasing x value is more or less related to the increase of phonon energy E_{ph}, see Figs. 1a and Figure 6. The position of the PL band follows a linear trend towards higher energies with increasing x value in $Sb_2(Se_{1-x}S_x)_3$, with an exception of x = 1 (Sb_2S_3), which shows a PL band at higher energies than the linear trend predicts. Considering also the low PL intensity of the Sb_2S_3 sample, we can propose that this sample has lower crystalline quality and may contain amorphous Sb_2S_3 phase, which has higher band gap (>1.8 eV [33]) compared to crystalline Sb_2S_3. The amorphous phase could result from non-optimized growth conditions for Sb_2S_3 as in this study the growth conditions were kept constant for the whole series of $Sb_2(Se_{1-x}S_x)_3$ solid solutions.

Finally, the temperature dependencies of the integrated intensities of the PL emissions of the $Sb_2(Se_{1-x}S_x)_3$ solid solutions with x ≤ 0.2 enabled to determine the thermal activation energies for the corresponding PL bands by fitting the experimental data with the theoretical expression [34]:

$$\Phi(T) = \frac{\Phi_o}{1 + \alpha_1 \cdot T^{3/2} + \alpha_2 \cdot T^{3/2} \cdot \exp\left(-\frac{E_a}{kT}\right)} \quad\quad 2$$

where α_1 and α_2 are the process rate parameters and E_a is the thermal activation energy. Thermal activation energies E_a = 15 ± 3 meV and E_a

= 11 ± 3 meV for the samples with x = 0 and x = 0.2, respectively, were obtained. These E_a values correlate nicely with the thermal quenching activation energies found in a recent study for the excitons and biexcitons [18], confirming that the PL emission in the $Sb_2(Se_{1-x}S_x)_3$ solid solutions with x ≤ 0.2 is of excitonic origin. Unfortunately, there were not enough experimental data points to determine the PL quenching of the solid solutions from x = 0.4 to 1.

4. Conclusion

In this study, the polycrystals of $Sb_2(Se_{1-x}S_x)_3$ solid solutions were successfully synthesized and the structural and luminescent properties of these materials were studied. The XRD and Raman analysis confirmed the formation of the full range of solid solutions. The low-temperature (T = 3 K) PL emission of $Sb_2(Se_{1-x}S_x)_3$ solid solutions excited with a pulsed UV laser was found to shift towards higher energies from 1.309 eV to 1.728 eV with increasing sulfur content. Laser power and temperature dependent PL study enabled to determine the origin of the PL emission in the respective samples as of excitonic origin in the samples with x = 0 and 0.2 and resulting from the DD-DA pairs recombination in the samples with x = 0.4 to 1. Consequently, a change in the radiative recombination mechanism was detected in the studied $Sb_2(Se_{1-x}S_x)_3$ with varying S/Se ratio.

CRediT authorship contribution statement

Mehmet Ender Uslu: Conceptualization, Data curation, Formal analysis, Writing – original draft, Writing – review & editing. **Rokas Kondrotas:** Writing – review & editing, Conceptualization. **Ramūnas Nedzinskas:** Conceptualization, Data curation, Writing – review & editing. **Olga Volobujeva:** Writing – review & editing, Supervision, Data curation, Conceptualization. **Kristi Timmo:** Conceptualization, Data curation, Writing – review & editing. **Marit Kauk-Kuusik:** Writing – review & editing, Resources, Conceptualization. **Jüri Krustok:** Conceptualization, Data curation, Formal analysis, Writing – original draft, Writing – review & editing. **Maarja Grossberg:** Writing – review & editing, Writing – original draft, Supervision, Resources, Funding acquisition, Formal analysis, Data curation, Conceptualization.

Declaration of competing interest

The authors declare that they have no known competing financial interests or personal relationships that could have appeared to influence the work reported in this paper.

PRG1023.

Appendix A. Supplementary data

Supplementary data to this article can be found online at https://doi.org/10.1016/j.mssp.2022.106571.

References

[1] F. Yan, T.J. Zhu, X.B. Zhao, S.R. Dong, Microstructures and thermoelectric properties of GeSbTe based layered compounds, Appl. Phys. A 88 (2007) 425–428, https://doi.org/10.1007/s00339-007-4006-9.

[2] Y. Zheng, Q. Zhang, X. Su, H. Xie, S. Shu, T. Chen, G. Tan, Y. Yan, X. Tang, C. Uher, G.J. Snyder, Mechanically robust BiSbTe alloys with superior thermoelectric performance: a case study of stable hierarchical nanostructured thermoelectric materials, Adv. Energy Mater. 5 (2015) 1401391, https://doi.org/10.1002/aenm.201401391.

[3] A.M. Farid, H.E. Atyia, N.A. Hegab, AC conductivity and dielectric properties of Sb_2Te_3 thin films, Vacuum 80 (2005) 284–294, https://doi.org/10.1016/j.vacuum.2005.05.003.

[4] E. Dönges, Z. Anorg, Über Chalkogenohalogenide des dreiwertigen Antimons und Wismuts. II. Über Selenohalogenide des dreiwertigen Antimons und Wismuts und über Antimon(III)-selenid Mit 2 Abbildungen, Allg. Chem. 263 (1950) 280–291, https://doi.org/10.1002/zaac.19502630508.

[5] X. Wang, R. Tang, C. Wu, C. Zhu, T. Chen, Development of antimony sulfide–selenide $Sb_2(S,Se)_3$-based solar cells, J. Energy Chem. 27 (2018) 713–721, https://doi.org/10.1016/j.jechem.2017.09.031.

[6] C. Chen, W. Li, Y. Zhou, C. Chen, M. Luo, X. Liu, K. Zeng, B. Yang, C. Zhang, J. Han, J. Tang, Optical properties of amorphous and polycrystalline Sb2Se3 thin films prepared by thermal evaporation, Appl. Phys. Lett. 107 (2015), 043905, https://doi.org/10.1063/1.4927741.

[7] V.L. Deringer, R.P. Stoffel, M. Wuttig, R. Dronskowski, Vibrational properties and bonding nature of Sb_2Se_3 and their implications for chalcogenide materials, Chem. Sci. 6 (2015) 5255, https://doi.org/10.1039/C5SC00825E.

[8] Y. Zhou, L. Wang, S. Chen, S. Qin, X. Liu, J. Chen, D.-J. Xue, M. Luo, Y. Cao, Y. Cheng, E.H. Sargent, J. Tang, Thin-film Sb_2Se_3 photovoltaics with oriented one-dimensional ribbons and benign grain boundaries, Nat. Photonics 9 (2015) 409–415, https://doi.org/10.1038/nphoton.2015.78.

[9] M. Huang, P. Xu, D. Han, J. Tang, S. Chen, Complicated and unconventional defect properties of the quasi-one-dimensional photovoltaic semiconductor Sb_2Se_3, ACS Appl. Mater. Interfaces 11 (17) (2019) 15564–15572, https://doi.org/10.1021/acsami.9b01220.

[10] C.N. Savory, D.O. Scanlon, The complex defect chemistry of antimony selenide, J. Mater. Chem. 7 (2019) 10739–10744, https://doi.org/10.1039/C9TA02022E.

[11] Z. Li, X. Liang, G. Li, H. Liu, H. Zhang, J. Guo, J. Chen, K. Shen, X. San, W. Yu, R.E. I. Schropp, Y. Mai, 9.2%-efficient core-shell structured antimony selenide nanorod array solar cells, Nat. Commun. 10 (2019), https://doi.org/10.1038/s41467-018-07903-6. Article number: 125.

[12] C. Chen, D.C. Bobela, Y. Yang, S. Lu, K. Zeng, C. Ge, B. Yang, L. Gao, Y. Zhao, M. C. Beard, J. Tang, Characterization of basic physical properties of Sb_2Se_3 and its relevance for photovoltaics, Front. Optoelectron. 10 (2017) 18–30, https://doi.org/10.1007/s12200-017-0702-z.

[13] R. Tang, Z.-H. Zheng, Z.-H. Su, X.-J. Li, Y.-D. Wei, X.-H. Zhang, Y.-Q. Fu, J.-T. Luoa, P. Fan, G.-X. Liang, Highly efficient and stable planar heterojunction solar cell based on sputtered and post-selenized Sb_2Se_3 thin film, Nano Energy 64 (2019) 103929, https://doi.org/10.1016/j.nanoen.2019.103929.

[14] C. Yuan, L. Zhang, W. Liu, C. Zhu, Rapid thermal process to fabricate Sb_2Se_3 thin film for solar cell application, Sol. Energy 137 (2016) 256–260, https://doi.org/10.1016/j.solener.2016.08.020.

[15] L. Guo, B. Zhang, S. Ranjit, J. Wall, S. Saurav, A.J. Hauser, G. Xing, L. Li, X. Qian, F. Yan Interface, Engineering via sputtered oxygenated CdS:O window layer for highly efficient Sb_2Se_3 thin-film solar cells with efficiency above 7, Solar RRL. 3 (2019) 1900025, https://doi.org/10.1002/solr.201900225.

[16] X. Wen, C. Chen, S. Lu, K. Li, R. Kondrotas, Y. Zhao, W. Chen, L. Gao, C. Wang, J. Zhang, G. Niu, J. Tang, Vapor transport deposition of antimony selenide thin film solar cells with 7.6% efficiency, Nat. Commun. 9 (2018) 2179, https://doi.org/10.1038/s41467-018-04634-6.

[17] M. Grossberg, O. Volobujeva, A. Penežko, R. Kaupmees, T. Raadik, J. Krustok, Origin of photoluminescence from antimony selenide, J. Alloys Compd. 817 (2020) 152716, https://doi.org/10.1016/j.jallcom.2019.152716.

[18] J. Krustok, R. Kondrotas, R. Nedzinskas, K. Timmo, R. Kaupmees, V. Mikli, M. Grossberg, Identification of excitons and biexcitons in Sb_2Se_3 under high photoluminescence excitation density, Adv. Opt. Mater. 9 (2021) 2100107, https://doi.org/10.1002/adom.202100107.

[19] Y. Zeng, K. Sun, J. Huang, M.P. Nielsen, F. Ji, C. Sha, S. Yuan, X. Zhang, C. Yan, X. Liu, H. Deng, Y. Lai, J. Seidel, N. Ekins-Daukes, F. Liu, H. Song, M. Green, X. Hao, Quasi-vertically-oriented antimony sulfide inorganic thin-film solar cells achieved by vapor transport deposition, ACS Appl. Mater. Interfaces 12 (20) (2020) 22825–22834, https://doi.org/10.1021/acsami.0c02697.

[20] N.N. Syrbu, V.V. Zalamai, I.G. Stamov, S.I. Beril, Excitonic and electronic transitions in Me–Sb_2Se_3 structures, Beilstein J. Nanotechnol. 11 (2020) 1045–1053, https://doi.org/10.3762/bjnano.11.89.

[21] L. Jiajun, L. Jianming, L. Congqiang, L. Wenquan, L. Shirong, S. Wenchao, Mineralogy of the stibnite-antimonselite series, Int. Geol. Rev. 41 (11) (1999) 1042–1050, https://doi.org/10.1080/00206819909465189.

[22] R. Kondrotas, C. Chen, X. Liu, B. Yang, J. Tang, Low-dimensional materials for photovoltaic application, J. Semiconduct. 42 (2021), 031701, https://doi.org/10.1088/1674-4926/42/3/031701.

[23] R. Tang, X. Wang, W. Lian, J. Huang, Q. Wei, M. Huang, Y. Yin, C. Jiang, S. Yang, G. Xing, S. Chen, C. Zhu, X. Hao, M.A. Green, T. Chen, Hydrothermal deposition of antimony selenosulfide thin films enables solar cells with 10% efficiency, Nat. Energy 5 (2020) 587–595, https://doi.org/10.1038/s41560-020-0652-3.

[24] N. Fleck, T.D.C. Hobson, C.N. Savory, J. Buckeridge, T.D. Veal, M.R. Correia, D. O. Scanlon, K. Durose, F. Jäckel, Identifying Raman modes of Sb_2Se_3 and their symmetries using angle-resolved polarised Raman spectra, J. Mater. Chem. 8 (2020) 8337–8344, https://doi.org/10.1039/D0TA01783C.

[25] P. Sereni, M. Musso, P. Knoll, P. Blaha, K. Schwarz, G. Schmidt, Polarization-dependent Raman characterization of stibnite (Sb_2S_3), AIP Conf. Proc. 1267 (2010) 1131, https://doi.org/10.1063/1.3482339.

[26] Y.A. Sorb, V. Rajaji, P.S. Malavi, U. Subbarao, P. Halappa, S.C. Peter, S. Karmakar, C. Narayana, Pressure-induced electronic topological transition in Sb_2S_3, J. Phys. Condens. Matter 28 (2016), 015602, https://doi.org/10.1088/0953-8984/28/1/015602.

[27] M. Birkett, W.M. Linhart, J. Stoner, L.J. Phillips, K. Durose, J. Alaria, J.D. Major, R. Kudrawiec, T.D. Veal, Band gap temperature-dependence of close-space sublimation grown Sb_2Se_3 by photo-reflectance, Apl. Mater. 6 (2018), 084901, https://doi.org/10.1063/1.5027157.

[28] T. Schmidt, K. Lischka, W. Zulehner, Excitation-power dependence of the near-band-edge photoluminescence of semiconductors, Phys. Rev. B 45 (1992) 8989, https://doi.org/10.1103/PhysRevB.45.8989.

[29] K. Huang, A. Rhys, Theory of light absorption and non-radiative transitions in F-centres, Proc. R. Soc. A 204 (1950) 406–423, https://doi.org/10.1142/9789812793720_0007.

[30] A.P. Levanyuk, V.V. Osipov, Edge luminescence of direct-gap semiconductors, Sov. Phys. Usp. 24 (1981) 187–215, https://doi.org/10.1070/PU1981v024n03ABEH004770.

[31] F. Williams, Donor—acceptor pairs in semiconductors, Phys. Status Solidi 25 (1968) 493–512, https://doi.org/10.1002/pssb.19680250202.

[32] J. Krustok, J. Raudoja, M. Krunks, H. Mändar, H. Collan, Nature of the native deep localized defect recombination centers in the chalcopyrite and orthorhombic $AgInS_2$, J. Appl. Phys. v. 88 (No 1) (2000) 205–209, https://doi.org/10.1063/1.373644.

[33] F. Aousgi, M. Kanzari, Study of the optical properties of the amorphous Sb_2S_3 thin films, J. Optoelectron. Adv. Mater. 12 (2) (2010) 227–232.

[34] J. Krustok, H. Collan, K. Hjelt, Does the low-temperature Arrhenius plot of the photoluminescence intensity in CdTe point towards an erroneous activation energy? J. Appl. Phys. 81 (1997) 1442–1445, https://doi.org/10.1063/1.363903.